Formation of localized sand patterns downstream from a vertical cylinder under steady flows: Experimental and theoretical study

Anthony Auzerais, Armelle Jarno, Alexander Ezersky, François Marin

Formation of localized sand patterns downstream from a vertical cylinder under steady flows: Experimental and theoretical study

Anthony Auzerais,[1] Armelle Jarno,[1] Alexander Ezersky,[2] and François Marin[1,*]

[1]*Laboratoire Ondes et Milieux Complexes, Université Le Havre Normandie, UMR CNRS 6294, 76600 Le Havre, France*

[2]*Laboratoire Morphodynamique Continentale et Côtière, Université Caen Normandie, UMR CNRS 6143, 14000 Caen, France*

(Received 26 May 2016; revised manuscript received 21 September 2016; published xxxxxx)

The generation of localized, spatially periodic patterns on a sandy bottom is experimentally and theoretically studied. Tests are performed in a hydrodynamic flume where patterns are produced downstream from a vertical cylinder under a steady current. It is found that patterns appear as a result of a subcritical instability of the water-sand bottom interface. A dependence of the area shape occupied by the patterns on the flow velocity and the cylinder diameter is investigated. It is shown that the patterns' characteristics can be explained using the Swift-Hohenberg equation. Numerical simulations point out that for a correct description of the patterns, an additional term which takes into account the impact of vortices on the sandy bottom in the wake of a cylinder must be added in the Swift-Hohenberg equation.

DOI: 10.1103/PhysRevE.00.002900

I. INTRODUCTION

In recent decades, the study of the formation of localized structures in nonequilibrium media has attracted the attention of researchers. Such structures were found in chemically active media, in granular materials, and in many numerical experiments with model equations. A sandy bottom under hydrodynamic flow is an example of a nonequilibrium medium [1]. The interface between the water flow and the sandy bottom is unstable owing to perturbations with zero phase velocity. This instability has been studied for over 100 years [2]. It was found that its development may lead to the generation of different stationary patterns at the bottom: roller structures, modulated rollers, and cellular structures consisting of a rhombus or squares. These structures were studied in detail for the case of supercritical instability when spatially periodic patterns arise from infinitesimal perturbations and occupy an area with a characteristic dimension that is substantially greater than the spatial period of the pattern. In this paper, we investigate localized patterns which appear on a sandy bottom as a result of subcritical instability under finite-amplitude perturbations. These perturbations are generated downstream from a vertical cylinder. It should be noted that erosion, so-called scour [3–5], appears in the vicinity of the cylinder. The features of the scour have been investigated in detail, since they are essential for the design of hydraulic structures [6–10]. The present work is devoted to sand structures appearing under the influence of vortices in the wake of a vertical cylinder. Vortices contribute to finite perturbations and initiate the pattern's development on the sandy bottom. The mechanism of occurrence of localized patterns is investigated in this paper. For the present experimental conditions, the water-sand boundary is stable with respect to small perturbations when there is no vertical cylinder placed on the bed.

This paper is organized as follows. In Sec. II, the experimental setup and results are presented. Section III is devoted to the theoretical approach. The theoretical results are compared with the experimental findings. The paper ends with conclusions in Sec. IV.

II. EXPERIMENTAL SETUP AND RESULTS

The experiments were conducted in a 10-m-long, 0.49-m-wide current flume. The mean water depth H was 0.2 m. Current was generated by a recirculating pump, as shown in Fig. 1.

The first series of tests was carried out without sediment and without a cylinder. An acoustic Doppler current profiler (ADCP) was used for these tests to get vertical profiles of the fluid velocity in the channel above the artificial bed which was hydraulically smooth. The flow regime was turbulent for all of the tests since the value of the flow Reynolds number $\mathrm{Re} = \overline{U}H/\upsilon$, where $\overline{U}$ is the depth-averaged current velocity and υ the water kinematic viscosity, was greater than 5000, the critical value for the flow to be turbulent [11]. The velocity profiles can be described by a logarithmic law characteristic of a turbulent flow, for $z > 0.02$ m, where z is the vertical distance above the bed (Fig. 2), except for the highest values of z where the outer flow takes place. This logarithmic law may be written as follows,

$$\frac{\overline{u}}{\overline{u}_*} = \frac{1}{K}\ln\left(\frac{z}{z_0}\right), \tag{1}$$

where $\overline{u}$ is the horizontal component of fluid velocity at height z above the bottom, $\overline{u}_*$ the shear velocity at the bed, K the Karman constant which is usually taken to be 0.4, and z_0 a length scale.

The test conditions are shown in Table I, where D is the cylinder diameter and $\mathrm{Re}_D = \overline{U}D/\nu$. Tests 1–13 were carried out with a 7-cm sand layer of median diameter $d = 340\ \mu$m and relative density $s = \rho_s/\rho = 2.65$, where ρ_s and ρ are the sand and fluid density, respectively, for flow conditions such as the bed shear stress was too weak to move the sediments when there was no vertical cylinder placed on the bottom. A critical value of 0.31 m/s for the depth-averaged current velocity $\overline{U}$ for the initial movement of the sediments has been experimentally obtained. Below this critical value, the sand particles on the

*francois.marin@univ-lehavre.fr

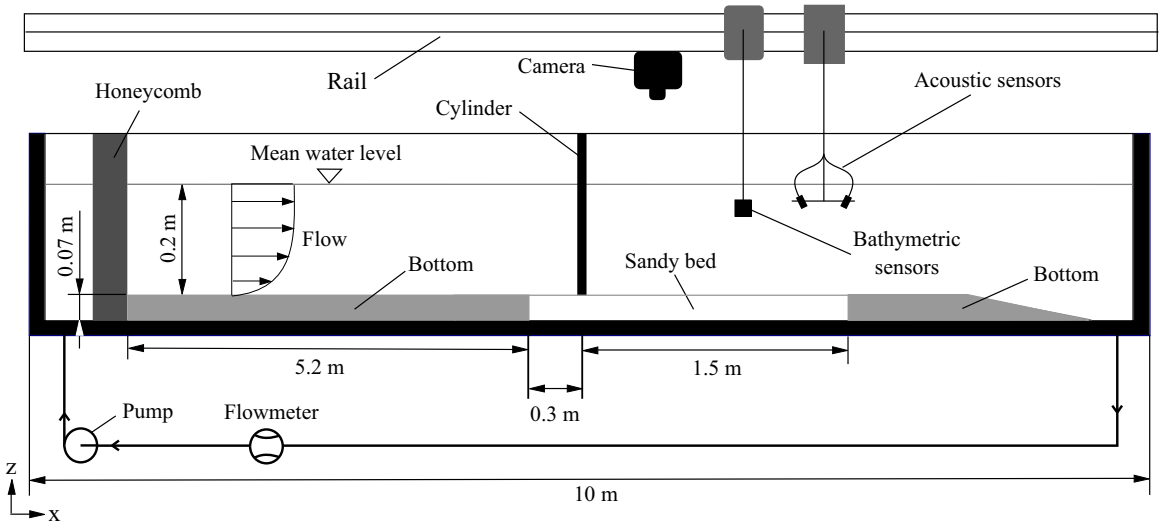

FIG. 1. The experimental setup.

bottom are motionless, when sediment transport starts above this value. Let us consider the following relation proposed by Ref. [12],

$$\theta_c = \frac{0.30}{1 + 1.2D_*} + 0.055[1 - \exp(-0.020D_*)], \qquad (2)$$

where θ_c is the critical value of the Shields parameter θ for the incipient sediment motion, and $D_* = [(s-1)g/\nu^2]^{1/3}d$, with g the acceleration due to gravity. The Shields parameter is defined as follows,

$$\theta = \frac{\tau_0}{\rho(s-1)gd}, \qquad (3)$$

where τ_0 is the bed shear stress. Using Eqs. (2) and (3), for the present tests, it is possible to estimate the critical Shields number $\theta_c = 0.035$, and the critical value of shear velocity at the bed $\overline{u}_{*c} = \sqrt{\tau_{0c}/\rho} = 0.0139$ m/s for the incipient sediment motion, with τ_{0c} being the corresponding critical value of τ_0. The value of the Reynolds number $\mathrm{Re}_* = \overline{u}_{*c}k_s/\nu = 11.8$, where $k_s = 2.5d$ [13] is the roughness length of the bed, lies in the transition region since $5 < \overline{u}_{*}k_s/\nu < 70$ [11], and the length scale z_0 in the log-law velocity distribution [Eq. (1)] may be estimated by [11]

$$z_0 = \frac{k_s}{30}\left[1 - \exp\left(-\frac{\overline{u}_{*c}k_s}{27\nu}\right)\right] + \frac{\nu}{9\overline{u}_{*c}}. \qquad (4)$$

The bottom is considered to be hydraulically smooth when $\mathrm{Re}_* < 5$, and hydraulically rough when $\mathrm{Re}_* > 70$. In the transition regime ($5 < \mathrm{Re}_* < 70$), we have [11]

$$\overline{U} = 2.5\overline{u}_* \ln\left(\frac{H}{2.72z_0}\right). \qquad (5)$$

Using Eqs. (2), (4), and (5), we get an estimation of the critical value of the depth-averaged current velocity $\overline{U}$ for an incipient sediment motion of 0.29 m/s. This result is in good agreement with the experimentally obtained value of 0.31 m/s. Table I shows that the present tests were carried out for $\overline{U} < 0.29$ m/s, in other words, for $\theta < \theta_c$. A vertical cylinder was embedded in the sand layer, as shown in Fig. 1. The sandy bottom was

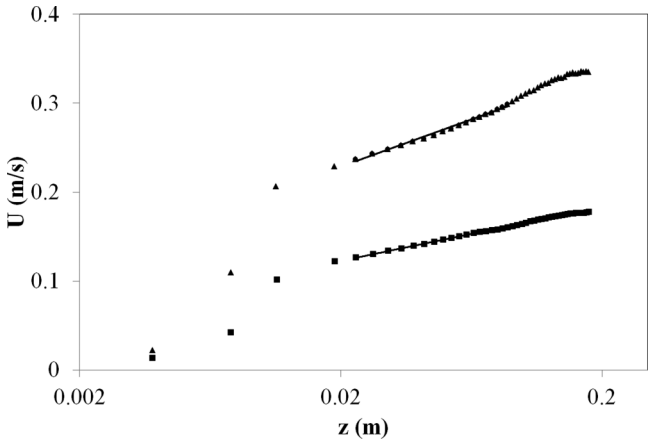

FIG. 2. Typical velocity profiles above the artificial smooth bed, without pile placed on the bed, for a horizontal distance from the honeycomb of 5 m. The solid lines show the best fit with the experimental data in the layer where the velocity profile is logarithmic. ■: Re = 29 000; ▲: Re = 53 000.

TABLE I. Experimental conditions.

Test number	D (mm)	$\overline{U}$ (m/s)	Re_D	Re
1	14	0.150	2100	30 000
2	14	0.190	2660	38 000
3	14	0.200	2800	40 000
4	14	0.210	2940	42 000
5	14	0.215	3010	43 000
6	25	0.150	3750	30 000
7	25	0.180	4500	36 000
8	25	0.185	4625	37 000
9	25	0.190	4750	38 000
10	25	0.195	4875	39 000
11	25	0.200	5000	40 000
12	25	0.210	5250	42 000
13	25	0.220	5500	44 000

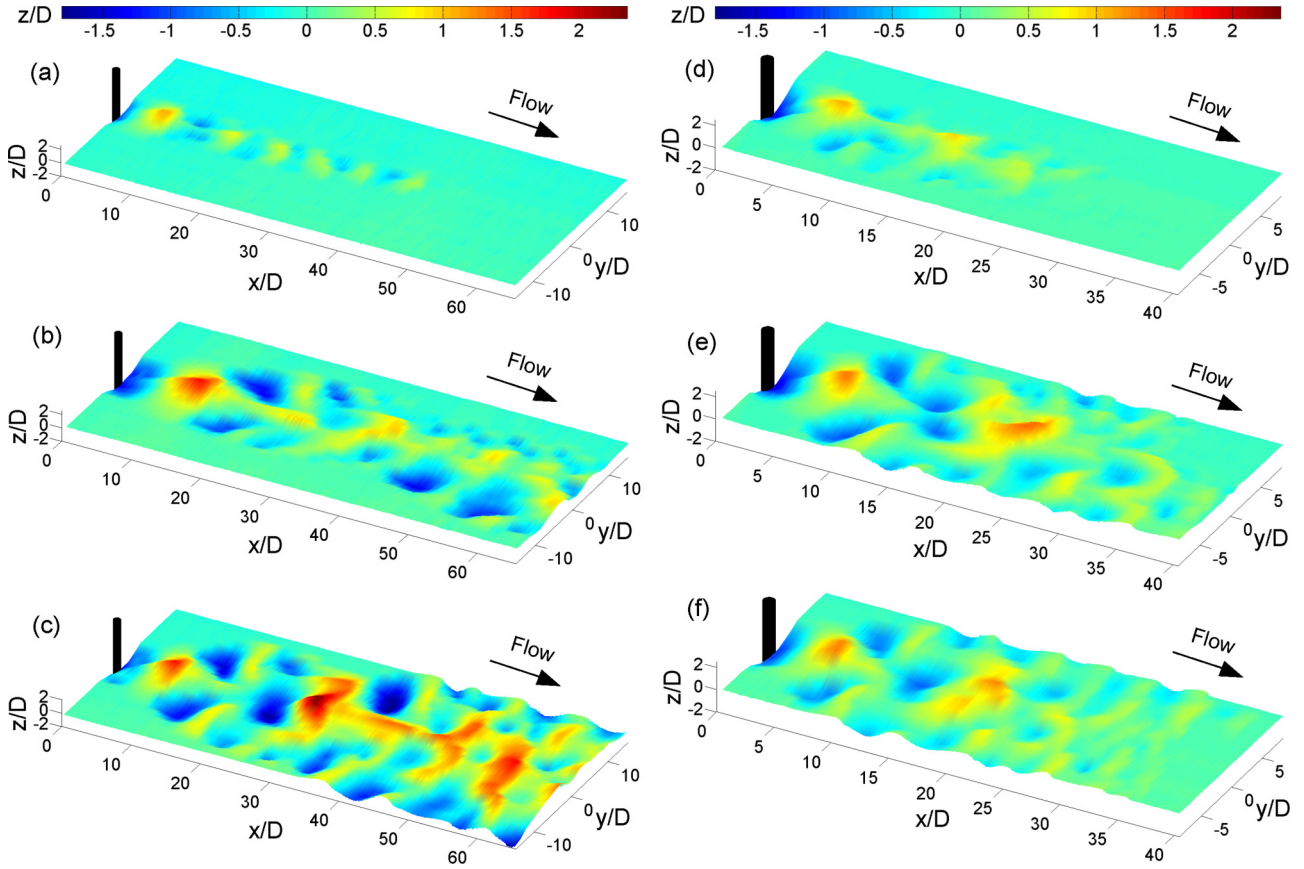

FIG. 3. Bed profiles at the equilibrium state. (a) Test 2, (b) test 4, (c) test 5, (d) test 8, (e) test 10, and (f) test 11.

initially flat. It is well known [8] that scour occurs in the vicinity of the cylinder such as

$$S_c = S\left[1 - \exp\left(-\frac{t}{t_*}\right)\right], \tag{6}$$

where S and S_c are the equilibrium scour depth and the value of the scour at time t, respectively, and t_* is the time scale of the scour process. The value of t_* may be estimated from the present tests at 30 min. For our experimental conditions, we have $2100 \leqslant \mathrm{Re}_D \leqslant 5500$ (see Table I), and a turbulent Karman vortex street occurs downstream from the vertical cylinder. Measurements carried out with hydrogen bubbles which were produced by electrolysis show that the dimensionless shedding frequency, the so-called Strouhal number $\mathrm{St} = fD/\overline{U}$, where f is the frequency of vortex shedding, is $\mathrm{St} \cong 0.2$. This value agrees well with well-known experimental data [14]. Bedforms appeared downstream from the cylinder due to vortices when the sediments did not move upstream from the cylinder (except in its vicinity where scour was observed), apart for tests 1 and 6 for which the bed remained flat. These two tests involve the lowest value of the depth-averaged current velocity, and the perturbations in the flow velocity field induced by the vortices are too weak to initiate the development of patterns. The intensity of these perturbations is considered later in this paper. A high-resolution camera was used to get the top views of the sand patterns, and an ultrasonic ranging system with a linear array of transducers mounted on a movable carriage was employed to provide three-dimensional (3D) bed profiles. Figure 3 depicts bed profiles obtained with the ultrasonic ranging system at the equilibrium state. The origins of x and y are located at the cylinder center. Sand patterns are clearly seen. For a fixed value of the cylinder diameter D, the area where patterns appear increases for increasing values of fluid flow velocity, as shown in Fig. 4 for $D = 25$ mm, figure displaying a sharp phase transition. For a given value of the depth-averaged current velocity $\overline{U}$, this area is enhanced for rising values of the cylinder diameter. This is illustrated in the comparison between experimental and theoretical results in the

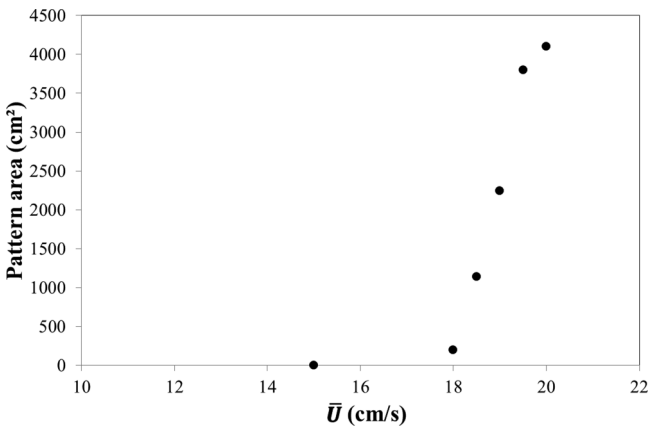

FIG. 4. Variation of pattern area with the depth-averaged current velocity at the equilibrium state. $D = 25$ mm.

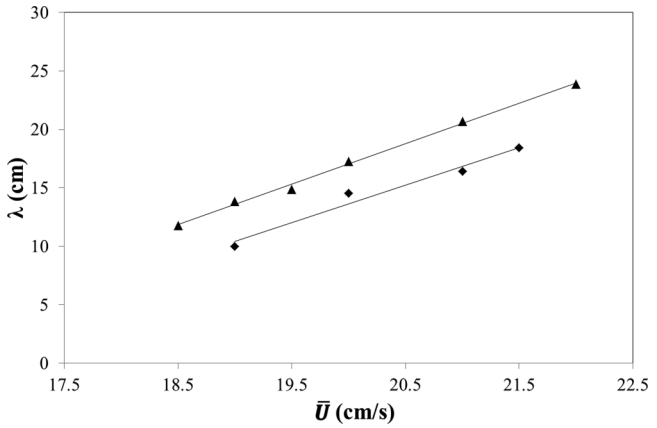

FIG. 5. Variation of the pattern wavelength with the depth-averaged current velocity at the equilibrium state. —♦—: $D = 14$ mm. · · · ▲ · · · : $D = 25$ mm.

following section of the paper (Figs. 13 and 15). The pattern wavelength λ can be easily obtained at the equilibrium state for the present tests. Figure 5, which exhibits a variation of λ with $\overline{U}$ for $D = 14$ mm and for $D = 25$ mm, shows that the pattern wavelength increases for increasing values of fluid flow velocity and of the cylinder diameter. Even at the equilibrium state, the patterns are never completely immobile. In this paper, we consider the patterns to be at the equilibrium state when the pattern characteristics no longer change significantly with time and fluctuate around the mean characteristics, as depicted in Fig. 6 for the pattern wavelength.

Lee-wake vortices induce perturbations in the velocity field which affect the bottom. Particle image velocimetry (PIV) measurements were carried out to estimate the level of these perturbations, as depicted in Fig. 7.

The measurements were performed without sediments on the bed, in a horizontal plane located at 0.02 m above a glass bottom, just outside the viscous sublayer. The camera was placed under the glass bed. The spatial resolution was 37 000 pixels/cm, and the acquisition frequency was 15 Hz. Figure 8 shows an example of the velocity field for the same flow conditions as test 11, but without sediments on the bed.

Perturbations in the velocity field due to the Lee-wake vortices are clearly exhibited. Time-averaged velocity fluctuation

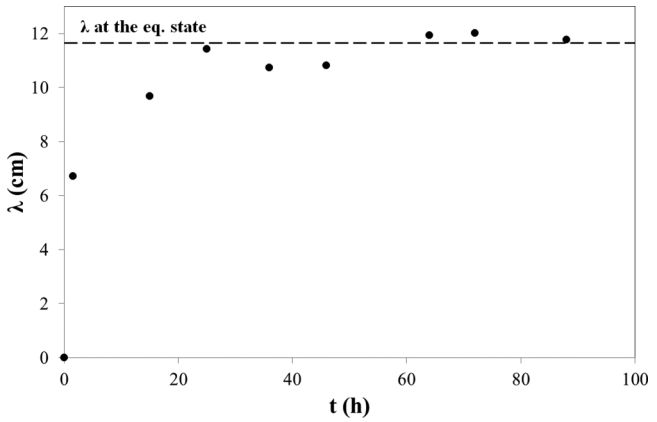

FIG. 6. Variation of the pattern wavelength with time t. Test 8.

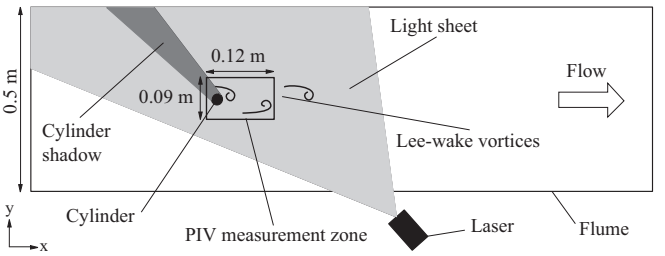

FIG. 7. Sketch of the particle image velocimetry (PIV) system.

fields were estimated using the following equation,

$$\widetilde{V}^2 = \frac{1}{T_i}\int_0^t \{(V_x - \overline{V}_x)^2 + (V_y - \overline{V}_y)^2\}dt, \qquad (7)$$

where V_x and V_y are the instantaneous velocity components along the x and y axis, respectively, $\overline{V_x}$ and $\overline{V_y}$ are the time-mean values of V_x and V_y, and $\widetilde{V}$ is the time-averaged velocity fluctuation. The integration time T_i was fixed to 16 s, which is a time window greater than ten times the time interval between two vortices shedding for all of the tests. Transverse profiles of $\widetilde{V}^2$ are depicted in Fig. 9 for $D = 14$ mm and $x/D = 1$. These profiles exhibit two peaks which correspond to the perturbations induced by the alternate vortex shedding downstream from the cylinder. For a fixed value of D, the intensity of the velocity fluctuations increases for increasing values of Re_D, as expected. Figure 9 shows that high values of the velocity fluctuations are located in the wake zone for $-1 \leqslant y/D \leqslant 1$. The variation of $\widetilde{V}^2$ with the dimensionless distance from the cylinder in the current direction x/D is plotted in Fig. 10 for $y/D = -0.3$ for the same tests as in Fig. 9. Figure 10 shows that, outside the immediate vicinity of the cylinder, the time-averaged velocity fluctuations decrease quite rapidly for increasing values of the distance x from the cylinder. As previously mentioned, no pattern appeared for test 1 when the patterns were generated for the other tests carried out with a 14 mm diam cylinder (tests 2–5). It can be deduced from Figs. 9 and 10 that for $D = 14$ mm, the patterns on the sandy bottom are not initiated under vortices when the peak values of $\widetilde{V}^2$ are lower than 0.008 $\mathrm{m}^2/\mathrm{s}^2$, approximately,

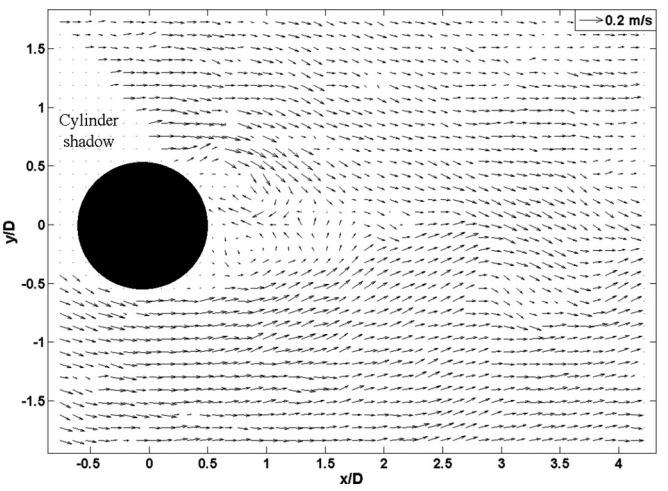

FIG. 8. Velocity field downstream from the cylinder. Re = 40 000, $\mathrm{Re}_D = 5000$ ($z = 0.02$ m).

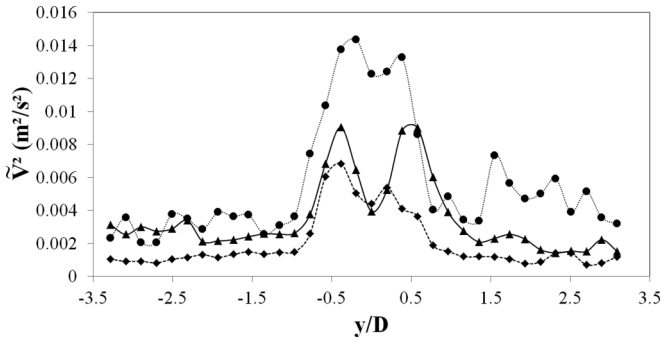

FIG. 9. Variation of $\widetilde{V}^2$ [Eq. (7)] with the dimensionless transverse distance from the cylinder y/D, for $x/D = 1$ ($z = 0.02$ m). -♦- -: $\mathrm{Re}_D = 2100$ (test 1). —▲—: $\mathrm{Re}_D = 2660$ (test 2). ···●···: $\mathrm{Re}_D = 3010$ (test 5).

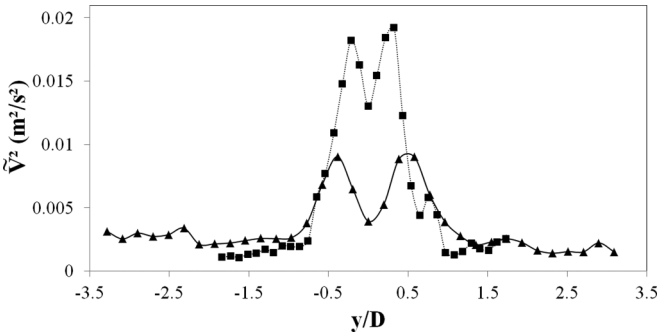

FIG. 11. Variation of $\widetilde{V}^2$ [Eq. (7)] with the dimensionless transverse distance from the cylinder y/D, for $x/D = 1$ ($z = 0.02$ m). $\overline{U} = 0.19$ m/s. —▲—: $D = 14$ mm (test 2). ···■···: $D = 25$ mm (test 9).

and that patterns appear when these values are greater than 0.008 $\mathrm{m}^2/\mathrm{s}^2$. In the case of the 25 mm diameter cylinder, the present tests indicate that patterns do not appear for peak values of $\widetilde{V}^2$ that are lower than 0.014 $\mathrm{m}^2/\mathrm{s}^2$, approximately, and do appear when these values are greater than 0.014 $\mathrm{m}^2/\mathrm{s}^2$ (figure not shown). This confirms that the considered instability leading to the formation of patterns on the sandy bottom downstream from a vertical cylinder is subcritical. For the same value of the fluid flow velocity, the time-averaged velocity fluctuations increase for increasing values of the cylinder diameter, as shown in Fig. 11 for $\overline{U} = 0.19$ m/s.

III. THEORETICAL APPROACH

Let us consider the Swift-Hohenberg equation [15], a phenomenological equation,

$$\frac{\partial u}{\partial T} = \varepsilon u - (1 + \overrightarrow{\nabla}^2)^2 u + q u^2 - u^3, \tag{8}$$

where u is the order parameter, $\overrightarrow{\nabla} = \overrightarrow{X}\frac{\partial}{\partial X} + \overrightarrow{Y}\frac{\partial}{\partial Y}$, X and Y are dimensionless distances in the horizontal plan, T is dimensionless time, q the coefficient for quadratic nonlinearity, and ε the linear instability of the system,

$$\varepsilon = \frac{\theta - \theta_c}{\theta}. \tag{9}$$

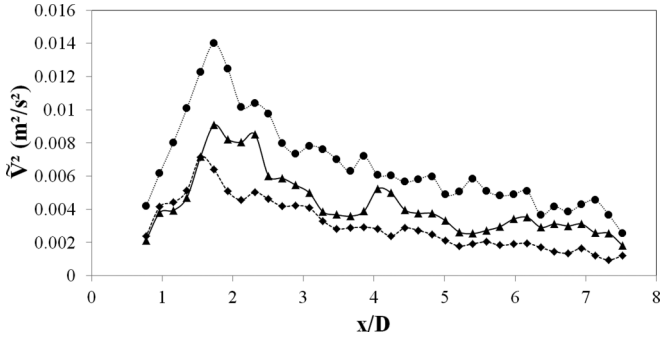

FIG. 10. Variation of $\widetilde{V}^2$ [Eq. (7)] with the dimensionless distance from the cylinder in the current direction x/D, for $y/D = -0.3$ ($z = 0.02$ m). - -♦- -: $\mathrm{Re}_D = 2100$ (test 1). —▲—: $\mathrm{Re}_D = 2660$ (test 2). ···●···: $\mathrm{Re}_D = 3010$ (test 5).

Instability to infinitesimal perturbations occurs if $\varepsilon > 0$. If $\varepsilon < 0$, linear instability is absent. The instability occurs for $q > 0$, if the initial perturbations are sufficiently large. It is the so-called subcritical instability appearing in many physical systems. The Swift-Hohenberg equation is widely used as a model to describe pattern formation [16,17]. In particular, it has been used to model patterns in fluids such as Rayleigh-Bénard convection.

Equation (8) describes patterns in media which are homogeneous for all directions in the ($\overrightarrow{X}$, $\overrightarrow{Y}$) plane. For example, the formation and dynamics of hexagonal or square cells may be explained by Eq. (8). In the present case, the system is anisotropic in the ($\overrightarrow{X}$, $\overrightarrow{Y}$) plane, a flow exists in one direction (X), and Eq. (8) can be modified to describe patterns observed in experiments in the following way,

$$\frac{\partial u}{\partial T} = \varepsilon u - \left[1 + \left(\frac{1}{k_0 D}\right)^2 \frac{\partial^2}{\partial X^2}\right]^2 u + D_Y \frac{\partial^2 u}{\partial Y^2} + q u^2 - u^3, \tag{10}$$

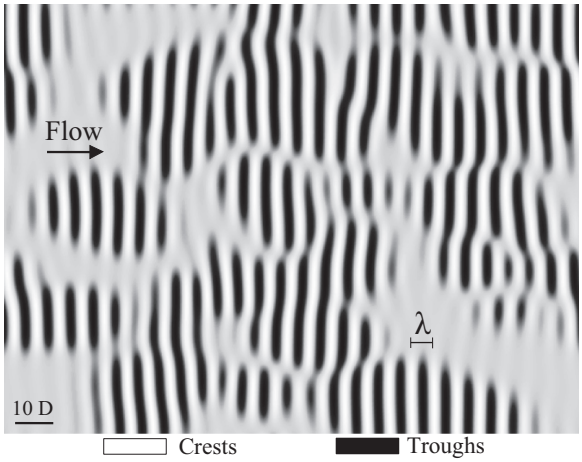

FIG. 12. Theoretical results [Eq. (10)] for $\varepsilon = 0.01$. $k_0 D = 1$, $D_Y = 1$, $q = 1.6$, 20 iterations.

where k_0 is the wave number, $k_0 = 2\pi/\lambda$, and D_Y a diffusion coefficient. For small positive values of ε, Eq. (10) depicts the instability of infinitesimal perturbations with wave numbers oriented along the X direction. This is confirmed by Fig. 12, representing results from Eq. (10) for $\varepsilon = 0.01$.

In our case, $\varepsilon < 0$ as our experiments are carried out in the subcritical regime, and patterns arise only in the wake of the cylinder where velocity and pressure perturbations initiate instability due to quadratic nonlinearity. We take into account these perturbations by adding a force $f(X,Y)$ corresponding to the time-averaged pressure forces acting on the sand-water interface on the right-hand side of Eq. (10):

$$\frac{\partial u}{\partial T} = \varepsilon u - \left[1 + \left(\frac{1}{k_0 D}\right)^2 \frac{\partial^2}{\partial X^2}\right]^2 u + D_Y \frac{\partial^2 u}{\partial Y^2} + q u^2 - u^3 + f(X,Y). \tag{11}$$

We suppose that this force is proportional to $\widetilde{V}^2$, where $\widetilde{V}^2$ is the spatially modulated random field defined by Eq. (7), because for the values of the Reynolds numbers Re_D (several thousands) involved in our experiments, a turbulent vortex street is observed. The fields of time-averaged velocity fluctuations $\widetilde{V}^2$ have been obtained just outside the viscous sublayer for the present tests, using the PIV method as described above. The shape of this force can be qualitatively explained as follows. Along a streamline, we can use the Bernoulli equation,

$$P + \rho \frac{\widetilde{V}^2}{2} = C, \tag{12}$$

where C is a constant. A pressure decrease is induced by an increase of the velocity. Therefore, low pressure corresponds to positive forces acting at the sand-water interface, and these forces introduce perturbations responsible for pattern formation. The diffusion coefficient D_Y [Eq. (10)] may be estimated from our experiments with the following equation,

$$D_Y = \left(\frac{l}{D}\right)^2 \frac{t_*}{t_{\mathrm{eq}}}. \tag{13}$$

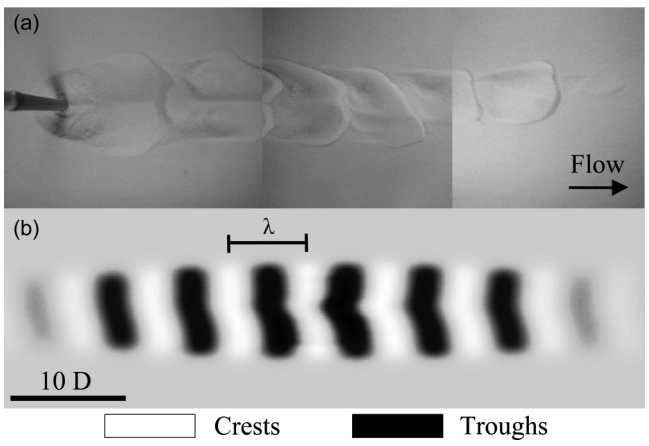

FIG. 13. Comparison between (a) experimental and (b) theoretical [Eq. (11)] results at the equilibrium state. Test 2. $\varepsilon = -0.182$, $k_0 D = 0.94$, $D_Y = 0.023$.

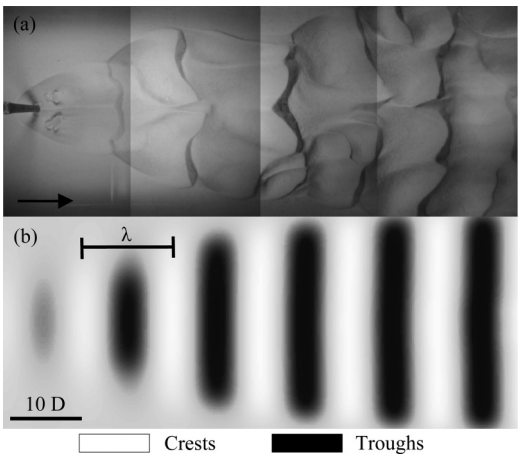

FIG. 14. Comparison between (a) experimental and (b) theoretical [Eq. (11)] results at the equilibrium state. Test 5. $\varepsilon = -0.172$, $k_0 D = 0.50$, $D_Y = 0.3$.

In this equation, l is half of the lateral extension (in the Y direction) of the sand pattern at the equilibrium state, and t_{eq} the time required to reach equilibrium. It should be noted that Eq. (11) can be written in the general gradient form

$$\frac{\partial u}{\partial T} = -\frac{\delta F}{\delta u}, \tag{14}$$

where F is the free-energy functional,

$$F = \int_\Omega \left\{ \frac{1}{2}\left[\left(1 + \left(\frac{1}{k_0 D}\right)^2 \frac{\partial^2}{\partial X^2}\right) u\right]^2 - D_Y \frac{1}{2}\left[\left(\frac{\partial}{\partial Y}\right) u\right]^2 - \varepsilon \frac{u^2}{2} - q\frac{u^3}{3} + \frac{u^4}{4} - f(X,Y)u \right\} dX dY, \tag{15}$$

and Ω is the two-dimensional region of space in which the pattern occurs. The time derivative of this free-energy functional gives us

$$\frac{\partial F}{\partial T} = -\int_\Omega \left(\frac{\partial u}{\partial T}\right)^2 dX dY \leqslant 0. \tag{16}$$

Free energy may only decrease as it evolves. The limiting behavior for gradient systems is either a steady attractor or propagating fronts. Using the Fourier spatial method, we numerically find nonhomogeneous steady states, as shown below.

Let us compare experimental and theoretical results at the equilibrium state. The value of the coefficient q is 1.6 for the present simulations, and the number of iterations is 500. Figures 13–15 depict the results for tests 2, 5, and 9,

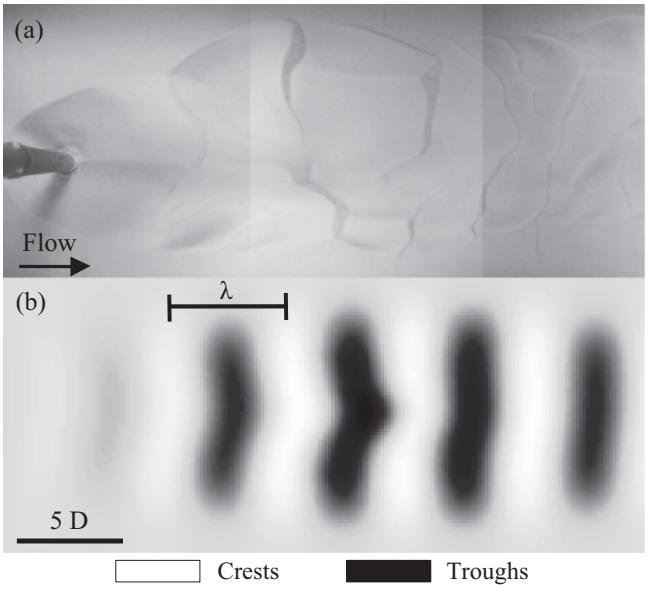

FIG. 15. Comparison between (a) experimental and (b) theoretical [Eq. (11)] results at the equilibrium state. Test 9. $\varepsilon = -0.182$, $k_0 D = 0.78$, $D_Y = 0.11$.

respectively. A reasonable agreement is obtained between the experimental and theoretical results. In particular, the spatial extension of patterns and the wavelength λ are well reproduced. It is not surprising to obtain a greater spatial extension for tests 5 and 9 than for test 2, since tests 5 and 9 involve higher fluid velocities and a larger cylinder diameter, respectively, leading to larger time-averaged velocity fluctuations, and then to a greater force $f(X,Y)$.

IV. CONCLUSIONS

The formation of localized sand patterns downstream from a vertical cylinder under turbulent steady flows is experimentally and theoretically studied. Tests which were carried out in a hydrodynamic flume depict the generation of patterns as a result of a subcritical instability of the water-sand interface. Lee-wake vortices induced by the cylinder lead to perturbations in the velocity field and to an additional force on the sandy bed. The present results show that localized steady states may be numerically obtained by using a modified Swift-Hohenberg equation with an additional term for this force. Numerically obtained pattern characteristics are in reasonable agreement with experimental observations.

ACKNOWLEDGMENT

The authors express their sincere thanks to the High Normandy region (Conseil Régional de Haute Normandie, GRR TERA, SCALE Research Network) for funding this work, and to Gaële Perret for her help with the PIV measurements.

[1] J. Lebunetel-Levaslot, A. Jarno-Druaux, A. B. Ezersky, and F. Marin, Phys. Rev. E **82**, 032301 (2010).
[2] S. Dey, *Fluvial Hydrodynamics: Sediment Transport and Scour Phenomena* (Springer, Berlin, 2014).
[3] H. N. C. Breusers, G. Nicollet, and H. W. Shen, J. Hydraul. Res. **15**, 211 (1977).
[4] A. W. Niedorada and C. Dalton, Ocean Eng. **9**, 159 (1982).
[5] G. J. C. M. Hoffmans and H. J. Verheij, *Scour Manual* (A. A. Balkema, Rotterdam, 1997).
[6] R. Whitehouse, *Scour at Marine Structures: A Manual for Practical Applications* (Thomas Telford Publishing, London, 1998).
[7] B. W. Melville and S. E. Coleman, *Bridge Scour* (Water Resources Publications, Colorado, 2000).
[8] B. M. Sumer and J. Fredsøe, *The Mechanics of Scour in the Marine Environment* (World Scientific, Singapore, 2002).
[9] R. Ettema, G. Constantinescu, and B. Melville, *Evaluation of Bridge Scour Research: Pier Scour Processes and Predictions* (Transportation Research Board, Washington, D.C., 2011).
[10] W. G. Qi and F. P. Gao, Sci. China: Technol. Sci. **57**, 1030 (2014).
[11] J. F. A. Sleath, *Sea Bed Mechanics* (Wiley, New York, 1984).
[12] R. L. Soulsby and R. J. S. Whitehouse, *Dynamics of Marine Sands* (Thomas Telford Publishing, London, 1997).
[13] P. Nielsen, *Coastal and Estuarine Processes* (World Scientific, Singapore, 2009).
[14] B. Etkin and H. S. Ribner, Canadian research in aerodynamic noise, University of Toronto, UTIA Rev. No. 13 (1958).
[15] J. Swift and P. C. Hohenberg, Phys. Rev. A **15**, 319 (1977).
[16] D. J. B. Lloyd, B. Sandstede, D. Avitabile, and A. R. Champneys, J. Appl. Dyn. Syst. **7**, 1049 (2008).
[17] M' F. Hilali, S. Métens, P. Borckmans, and G. Dewel, Phy. Rev. E **51**, 2046 (1995).